AGU PUBLICATIONS

JGR

Journal of Geophysical Research: Solid Earth

RESEARCH ARTICLE
10.1002/2016JB013046

Key Points:
- Virtual deep seismic sounding (VDSS) tightly constrains crustal buoyancy and residual topography
- Residual topography in the western U.S. is significant and highly variable
- Joint analyses of VDSS and conventional receiver functions provide further constraints on crustal properties

Supporting Information:
- Supporting Information S1

Correspondence to:
C. Yu,
yucq@mit.edu

Citation:
Yu, C., W.-P. Chen, and R. D. van der Hilst (2016), Constraints on residual topography and crustal properties in the western United States from virtual deep seismic sounding, *J. Geophys. Res. Solid Earth*, *121*, 5917–5930, doi:10.1002/2016JB013046.

Received 31 MAR 2016
Accepted 25 JUL 2016
Accepted article online 29 JUL 2016
Published online 17 AUG 2016

Constraints on residual topography and crustal properties in the western United States from virtual deep seismic sounding

Chunquan Yu[1], Wang-Ping Chen[2,3], and Robert D. van der Hilst[1]

[1]Department of Earth, Atmospheric and Planetary Sciences, Massachusetts Institute of Technology, Cambridge, Massachusetts, USA, [2]Ocean College, Zhejiang University, Hangzhou, China, [3]Formerly at Department of Geology, University of Illinois at Urbana-Champaign, Urbana, Illinois, USA

Abstract We use virtual deep seismic sounding (VDSS) and data from ~1000 broadband seismic stations to provide high-resolution estimates of crustal structure in the western Cordillera of the United States (U.S.). The most robust result is the geographic distribution of residual topography (that is, the difference between observed elevation and that expected from crustal buoyancy alone) and, by implication, thermal or petrologic anomalies in the mantle. Overall, residual topography of the western U.S. Cordillera varies considerably; with contrasts of up to about 3 km across distances of 200 km or less. High residual topography, indicating large mantle effects, is evident along the periphery of the Colorado Plateau and the surroundings of the Great Basin. In contrast, the central Colorado Plateau and the Wyoming Basin show low residual topography, close to what is expected of a geologically stable lithosphere. Overall, in regions to the east of the Wasatch hinge line (the eastern limit of significant extension in the North American cratonic basement) patterns of high residual topography and anomalies of low seismic wave speeds in the upper mantle are similar, suggestive of a common, thermal origin. In contrast, such a similarity is absent in regions to the west of the hinge line, suggesting substantial effects of petrological heterogeneities in the mantle. Finally, joint analyses of VDSS and conventional receiver functions reveal a wide range of crustal *P* wave speeds, locally as high as 6.7 km/s, perhaps indicating magmatic modification of the crust.

1. Introduction

The elevation of the western United States (U.S.)—the broadest part of the active Cordillera of western North America—is on average about 1 km higher than the stable North American craton to the east (Figure 1). Previous geophysical investigations suggest, however, that the underlying crust of the former is about 10 km thinner than that of the latter [e.g., *Chulick and Mooney*, 2002]. This suggests that the western U.S. is not in Airy isostatic equilibrium, so other geodynamic processes must be involved in maintaining the high elevation of this area. A natural candidate is thermal buoyancy due to anomalously warm upper mantle below the crust [e.g., *Thompson and Burke*, 1974]. This notion is supported by high surface heat flow [*Blackwell and Richards*, 2004] and reduced seismic wave speeds in the upper mantle [*Buehler and Shearer*, 2010; *Burdick et al*., 2010; *Schmandt and Humphreys*, 2010; *Shen et al*., 2013].

Hyndman and Currie [2011] estimated that to the first order, about 1600 m of elevation can be explained by a broad thermal anomaly over the entire region. However, the relative contribution of crustal buoyancy and thermal expansion of the upper mantle to support surface elevation of distinct geological/physiographic domains is not well established. Furthermore, the relative contributions from dynamic forces versus static buoyancy are also being debated (cf. *Lowry et al*. [2000] and *Becker et al*. [2013] with *Hyndman and Currie* [2011] and *Levandowski et al*. [2014]). Isolating and quantifying different contributions to surface topography requires better knowledge of crustal buoyancy, which, in turn, necessitates better constraints on crustal structure and properties.

Early seismological investigations of the crust in the western U.S. mostly relied on seismic refractions and reflections using man-made ("active") sources [e.g., *Chulick and Mooney*, 2002]. In principle, these methods can provide high-resolution images of the crust, but in many cases the signals are not sufficiently energetic to penetrate deep into the lithosphere or the data are too complicated to model in detail. In addition, the spatial coverage is often limited due to the high cost of such investigations. Recently, with

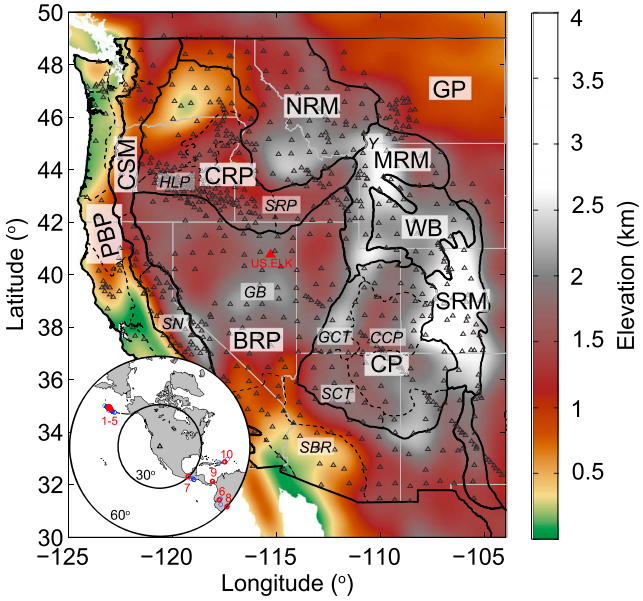

Figure 1. A color-coded topographic map [*USGS*, 1993], showing major physiographic provinces of the western United States [*Feneman*, 1931]. Small-scale topographic features are suppressed by applying a low-pass filter with a cutoff wavelength of $\lambda = 200$ km. Major physiographic boundaries are marked as thick, dark curves. BRP, Basin and Range province; CP, Colorado Plateau; CRP, Columbia River Plateau; CSM, Cascade-Sierra Mountains; GP, Great Plains; MRM, Middle Rocky Mountains; NRM, Northern Rocky Mountains; PBP, Pacific Border province; SRM, Southern Rocky Mountains; and WB, Wyoming Basin. Subphysiographic boundaries are marked as dashed curves. CCP, Central Colorado Plateau; GCT, Great Basin-Colorado Plateau transition; GB, Great Basin; HLP, High Lava Plains; SBR, Southern Basin and Range province; SCT, Southern Basin Range-Colorado Plateau transition; SN, Sierra Nevada; SRP, Snake River Plains; and Y, Yellowstone. Broadband seismic stations used in this study are shown as open triangles. Red triangle marks the location of station US.ELK whose data are shown in Figure 2c. Inset at the lower left corner is a map (in equidistant azimuthal projection) showing the distribution of the events (red dots) used for VDSS. The center of projection is at station US.ELK, with the events numbered as in Table 1. Small blue circles are auxiliary events used for calculating relative *S* wave traveltime residuals (Figure S5).

the deployment of the USArray component of the EarthScope initiative, conventional receiver functions (CRFs) have been widely used to map the structure of the crust across the western U.S. [e.g., *Lowry and Perez-Gussinye*, 2011; *Gilbert*, 2012; *Levander and Miller*, 2012]. This method uses a portion of the wavefield that is produced by scattering of teleseismic *P* waves near seismic stations and constrains structures at greater depths and over larger areas than active source studies (see more discussions in the next section). In addition, the dispersion of surface waves, either generated by natural earthquakes or estimated from ambient noise, has also been applied to study shear wave structures in the crust with a broad spatial coverage [e.g., *Yang et al.*, 2008]. CRFs and surface wave data can also be combined to improve constraints on crustal shear wave speed [*Shen et al.*, 2013].

However, these studies are of limited use in estimating how much topography is supported by crustal buoyancy or by other sources. Birch's law, which describes a linear relationship between *P* wave speed and density for crustal rocks [*Birch*, 1961; *Christensen and Mooney*, 1995; *Brocher*, 2005], can be used to constrain crustal buoyancy if we know both the average speed of *P* wave and the overall thickness of the crust. However, CRFs and surface wave dispersion both have little sensitivity to crustal *P* wave speed. Lately, *Lin et al.* [2012] reported that the ellipticity, or the amplitude ratio between horizontal and vertical components of particle motions, of Rayleigh wave has some sensitivity to density, but this application is limited to the uppermost crust.

For the estimation of crustal *P* wave speed and thickness, and particularly buoyancy, virtual deep seismic sounding (VDSS) [*Tseng et al.*, 2009; *Yu et al.*, 2012, 2013] has several distinct advantages over other methods. First, VDSS returns a robust signal from the crust-mantle boundary even if the Moho is complicated or transitional in nature [*Tseng et al.*, 2009]. Second, VDSS is not particularly susceptible to signal-generated noise such as scatterings from thick sediments or intracrustal discontinuities [*Yu et al.*, 2012]. Last and most important, as will be shown here, VDSS can be used to put tight constraints on crustal buoyancy in spite of an inherent trade-off between overall crustal thickness and *P* wave speed.

In this paper, we first summarize the key points of VDSS and then discuss how the method is used to constrain crustal buoyancy. We apply VDSS to broadband seismic waveforms collected by the USArray and other deployments and provide high-resolution estimates of crustal buoyancy and in some cases additional constraints on bulk crustal properties in the western U.S.

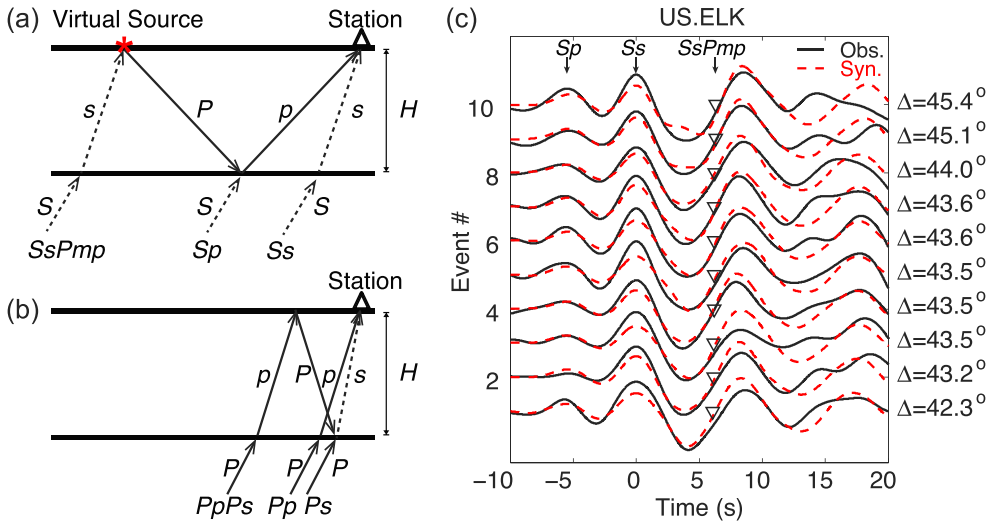

Figure 2. (a) A schematic diagram illustrating raypaths of major seismic phases associated with an incoming teleseismic *S* wave near a station. The difference in timing between wide-angle reflection off the Moho, phase *SsPmp*, and the direct phase, *Ss*, is the key in virtual deep seismic sounding (VDSS). (b) A corresponding plot for an incoming teleseismic *P* wave. Conventional receiver functions focus on the primary *P*-to-*S* conversion across the Moho (*Ps*). A number of related multiples, such as *PpPs* and *PpSs* + *PsPs* (not shown to avoid clutter), are potentially useful. (c) Examples of seismograms from a cluster of 10 different events recorded by the station US.ELK in the northern Great Basin (Figure 1). Dashed curves are synthetic seismograms that match the observations well (solid curves). Each observed waveform is proportional to the vertical component of ground velocity, after two-pass filtering between the passband of 0.02–0.3 Hz. Consistency among waveforms at similar ray parameters and the large amplitude of the *SsPmp* phase highlight the robustness of VDSS. Note that at these epicentral distances (Δ), the *SsPmp* phase is a postcritical reflection whose phase is shifted relative to the *Ss* phase. Seismograms are aligned along the onset of the *Ss* phase, and inverted triangles mark arrivals of the *SsPmp* phase.

2. Data and Methods

2.1. VDSS

VDSS focuses on the phase *SsPmp*, a prominent signal that originates as an *S*-to-*P* conversion at the free surface near the receiver. The conversion acts as a virtual source for the subsequent reflection off the Moho (Figure 2a). For layered, isotropic media, the differential timing between *SsPmp* and direct *S*, or *Ss*, is related to the crustal thickness *H* and average *P* wave speed in the crust, V_P, as follows:

$$T_{SsPmp-Ss} = 2H\left(V_P^{-2} - p_\beta^{2}\right)^{1/2}, \quad (1)$$

where p_β is the ray parameter (horizontal slowness) of the incident *S* wave. At distances less than about 55°, p_β is large enough to cause a postcritical *P* reflection off the Moho, resulting in a signal with an amplitude that is comparable to that of the direct *S* phase on the vertical component of seismograms. A distance of ~30° is used as a practical lower limit to avoid triplications caused by major discontinuities that bound the transition zone of the mantle. Within this range of distances, the phase *SsPmp* is a wide-angle reflection and the distance between the virtual source and the receiver is about twice the crustal thickness (Figure 2a).

In comparison, CRFs mainly rely on the *Ps* phase or the *P*-to-*S* wave conversion across the Moho (Figure 2b) [e.g., *Ammon*, 1991]. The differential timing between *Ps* and the direct *P* phase, or *Pp*, is

$$T_{Ps-Pp} = H\left(\left(V_S^{-2} - p_\alpha^{2}\right)^{1/2} - \left(V_P^{-2} - p_\alpha^{2}\right)^{1/2}\right), \quad (2)$$

where p_α is the ray parameter of the incident *P* wave and V_S the average crustal *S* wave speed. Note that the precritical nature of the *Ps* phase and related multiples results in weak amplitude of these phases. When the *Ps* phase is clear on CRFs, equation (2) can be used in conjunction with equation (1) for joint determination of both *H* and V_P, provided that there are additional constraints on crustal V_P/V_S or, equivalently, the Poisson's ratio (supporting information).

The high signal-to-noise ratio of the *SsPmp* phase used in VDSS is advantageous in several ways. First, it negates the need to stack data from a large number of events, a practice typically needed for CRFs.

Table 1. Ten Key Events for VDSS

Source Region	Event No.	Date[a]	Origin Time (UT)	Latitude (°N)	Longitude (°E)	Depth (km)	Magnitude (M_w)
Aleutian subduction zone	1	2007-04-29	12:41:57.4	52.01	−179.97	117	6.2
	2	2007-7-13	21:54:43.1	51.84	−176.28	35	6.0
	3	2007-10-31	13:44:19.8	51.42	−178.38	28	6.0
	4	2007-12-21	07:24:34.0	51.37	−178.98	25	6.3
	5	2008-3-22	21:24:11.3	52.18	−178.72	132	6.2
Central and South America	6	2007-11-16	03:13:00.1	−2.31	−77.84	123	6.8
	7	2008-2-12	12:50:18.5	16.36	−94.30	83	6.5
	8	2008-8-26	21:00:36.6	−7.64	−74.38	154	6.4
	9	2009-7-04	06:49:35.5	9.59	−78.97	38	6.1
	10	2010-5-16	05:16:10.0	18.40	−67.07	113	5.8

[a]Event catalog is the Preliminary Determination of Epicenters of the USGS.

Second, the *SsPmp* phase is not easily obscured by signal-generated noise, such as reverberations caused by near-surface sediments and reflections/ conversions across second-order crustal structures. Third, previous work has shown that even when the Moho interface is complicated or transitional in nature the *SsPmp* phase still gives a robust estimate of mean crustal thickness [*Tseng et al*., 2009].

The main source of data in our study is the archive of broadband seismograms from EarthScope, including those from the Transportable Array and Flexible arrays of the USArray, supplemented by those from other permanent and temporary deployments in the western U.S. (Figure 1). We select seismograms with clear *Ss* and *SsPmp* phases generated by significant events (moment magnitude $M_w \geq 5.7$) that occurred between 1997 and 2010 within distances of 30°–55° from receivers. The natural distribution of seismicity dictates that suitable events are associated with subduction zones either along the Aleutians or in Central and South America (inset in Figure 1). Table 1 lists the 10 best events for our purpose. Figure 2c demonstrates the consistency of relevant waveforms recorded at the same station from (spatially) nearby events. Moreover, the dense and regular distribution of seismic stations compensates for the limited azimuthal distribution of seismic sources, resulting in even coverage throughout the western U.S. (see results in the next section).

In order to measure $T_{SsPmp\text{-}Ss}$ reliably, we compare observed and synthetic seismograms (Figure 2c). For the latter, we approximate the *S* wave source wavelet, which includes both the source time-function and source-side scattering, by using the observed "pseudo-*S*" wave train obtained through the analysis of particle motions (supporting information; Figure S1) [*Yu et al*., 2013]. We then convolve the source wavelet with receiver side structural response calculated using the reflectivity method [*Randall*, 1989]. As shown by waveform modeling of *Tseng et al*. [2009] and *Yu et al*. [2012], details of crustal structure are not important for fitting the waveforms of both the *SsPmp* and the *Ss* phases, so we use only a single crustal layer in waveform modeling. In each case, $T_{SsPmp\text{-}Ss}$ is then determined by a best fitting synthetic seismogram among those generated from a suite of crustal models where $T_{SsPmp\text{-}Ss}$ is known through equation (1). We use the *Pn* tomography results of *Buehler and Shearer* [2010] as a reference for *P* wave speed of the uppermost mantle.

In most cases, modeling only the vertical component of seismogram is sufficient to determine the timing of both relevant phases. For stations situated on thick sediments we determine the timing of the *SsPmp* and *Ss* phases from the vertical and radial components of ground velocity, respectively. This practice is guided by the principle that raypaths of both phases should be near vertical because of the extremely low wave speeds in sediments. Thus, particle motions of *SsPmp* and *Ss* phases are expected to be close to vertical and radial, respectively. In addition, strong *S*-to-*P* conversions at the base of the sedimentary layer would produce discernible precursors to the *Ss* phase on the vertical component, leading to an undesirable uncertainty in the timing of *Ss*. In our practice, the typical uncertainty in $T_{SsPmp\text{-}Ss}$ is about ±0.4 s (one standard deviation; Figure S1), corresponding to about ±2 km in estimated crustal thickness.

2.2. Correction and Normalization of $T_{SsPmp\text{-}Ss}$

A potential source of error in the conversion of measured $T_{SsPmp\text{-}Ss}$ (hereinafter referred to as *T* for simplicity) to crustal thickness is small-scale heterogeneity in the crust and the uppermost mantle between the virtual source and the seismic station. For instance, if the *Ss* portion of the *SsPmp* phase passes through near-surface

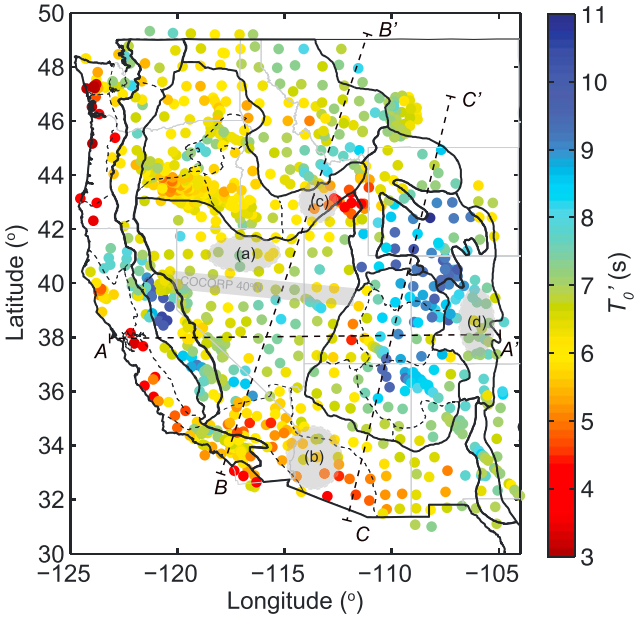

Figure 3. A map showing observed differential travel times between *SsPmp* and *Ss* phases, after correcting for traveltime residuals of the latter and normalizing to a common, reference *S* wave ray parameter of 0.1316 s/km. Each value is plotted at where the reflection off the Moho is expected, assuming a constant crustal *P* wave velocity of 6.3 km/s. Shaded ellipses, labeled as (a)–(d), mark the approximate locations of stations used in the joint analyses of VDSS and CRFs (Figure 7). Shaded box in the Great Basin shows the approximate location of the COCORP seismic reflection transect along 40°N [*Klemperer et al.*, 1986].

structures that are distinct from those directly under the station sampled by the (direct) *Ss* phase, then a correction to *T*, equivalent to the static correction in exploration seismology, is needed. For VDSS, subcrustal, small-scale heterogeneity, whose length scale is of the same order as the distance between the virtual source and the seismic station, would cause a similar effect (Figure 2a). These corrections are necessary, because (for the region considered here) traveltime tomography with USArray data yields up to ~5% and ~10% variations in *P* and *S* wavespeed, respectively, at depths between 60 and 120 km and over distances of about 100–200 km [*Burdick et al.*, 2010; *Schmandt and Humphreys*, 2010].

To mitigate this source of uncertainty, we measure arrival times of the direct *S* phase from each of the events shown in Table 1. We further expand this data set with auxiliary, high-quality events of $M_w \geq 5.5$ that occurred close to each of the events in Table 1 (Figure 1). For each event-station pair we calculate the *S* wave traveltime residual relative to the standard, global traveltime model *iasp91*. Since only the relative traveltime at each of the virtual source-station pair matters, the mean of measured traveltime residuals at all stations from a given event is removed. The final outcome for all events listed in Table 1 is shown in Figure S5. Note that events #1–5 occurred close to each other, so Figure S5a shows the complete result for all five events from the Aleutian subduction zone.

We then adjust each value of *T* according to the difference in traveltime residual, Δt, between the *Ss* phase at each station and the *Ss* portion of the *SsPmp* phase at each virtual source (Figure 2a). To this end, the former is directly measured at each location (Figure S5) and the latter is based on linear interpolations among relevant stations. As we assume that variations in traveltime residuals between nearby stations are smooth, the accuracy of this procedure is limited by station spacing. The corrected differential travel time between *SsPmp* and the *Ss* phases, *T*′, is

$$T' = T + \Delta t. \tag{3}$$

Since the exact location of the virtual source also depends on crustal thickness, Δt and *T*′ are jointly updated each time a preliminary estimate of *H* is calculated. Notice that this correction contains all major differences between the *Ss* portion of the two relevant phases, including effects both near the surface and at greater depths. By largely removing effects of lateral variations in *S* wave speeds, the assumption of lateral homogeneity in equation (1) remains valid for estimating crustal thickness from *T*′. The correction Δt is important for regions with strong gradient in traveltime residuals, such as portions of the Colorado Plateau and the Wyoming Basin, where it can reach up to 3 s, corresponding to ~15 km in crustal thickness estimation.

To account for variations in *T*′ that naturally arise from different distances (equivalent to the effect of moveout in exploration seismology [*Sheriff and Geldart*, 1995]), we further normalize all *T*′ to a common reference ray parameter, $p_{\beta 0}$, as follows:

$$T_0' = T'\left(V_P^{-2} - p_{\beta 0}^{\ 2}\right)^{1/2} / \left(V_P^{-2} - p_\beta^{\ 2}\right)^{1/2}, \tag{4}$$

where T_0' is the normalized (moveout corrected) value of T', and $p_{\beta 0}$ the reference S wave ray parameter (set to 0.1316 s/km). Using ray theory as a first approximation and assuming that the crust-mantle transition is characterized by P wave speeds that increase downward, critical reflection occurs when P wave speed of the upper mantle reaches 7.6 km/s for $p_{\beta 0}$. The exact value of V_P, the other parameter in equation (4), has a negligible effect on T_0'.

3. Spatial Distribution of T_0'

Figure 3 shows a map of measured T_0', with each value plotted at the (estimated) location of the Moho reflection. The results cover the western U.S. Cordillera at an average spacing of about 50 km between data points, suggesting that features with characteristic scales of at least 100 km are spatially unaliased. Higher resolution is reached at places where seismic data from dense arrays are available, such as in the High Lava Plains. We infer strong lateral variations in T_0', ranging from ~3 s to 11 s, and the spatial distribution shows a rough correlation with physiographic provinces (Figure 3). We will focus on regions to the east of the Cascade-Sierra Mountains because data coverage in the Pacific Border province is generally sparse.

Large values of T_0' are prevalent in the Colorado Plateau and the Wyoming Basin—two stable blocks in the western U.S. with thermal ages dating back to the Proterozoic and the Archean, respectively [*Burchfiel et al.*, 1992]. Values of T_0' in these two regions are relatively uniform, with an average of ~9 s (Figures 3, 4a, and 4c). However, except along its northern margin, decreases of T_0' are evident along the periphery of the Colorado Plateau on all other sides (Figures 3, 4a, and 4c). For example, T_0' values in the high Southern Rocky Mountain are smaller than those on the central Colorado Plateau by about 1 ~ 2 s (Figures 3 and 4a).

Relatively uniform values of T_0' (~7 s) are observed in the Great Basin, or the northern Basin and Range province—the most prominent expression of Cenozoic extension in the western U.S. Values of T_0' here are systematically larger than those measured in its southern counterpart, where T_0' gradually increases northeastward from ~5 s to ~7 s (Figures 3 and 4c). Locally, large values of T_0' are detected near the Death Valley (~36°N, 117°W; Figures 3 and 4b), within the so-called "amagmatic corridor" where the onset of Cenozoic extension is later and volcanism is less voluminous than other parts of the Basin and Range province [*Wernicke et al.*, 1987; *Schulte-Pelkum et al.*, 2011].

The margins of the Great Basin typically show smaller T_0' than the interior (Figures 3, 4a, and 4b). To the north, T_0' decreases to only ~5 s and ~6 s in the Eastern Snake River Plain and the High Lava Plains, respectively. Along the transition between the Great Basin and the Colorado Plateau, T_0' is ~5.5 s. To the west, T_0' is ~6 s in the eastern flanks of the central Sierra Nevada.

4. Crust and Mantle Support of Topography

4.1. Constraining Crustal Buoyancy

The contribution of crustal buoyancy to surface topography, h_c, is proportional to both crustal thickness (H) and the contrast in density between the crust and the asthenosphere [*Lachenbruch and Morgan*, 1990]:

$$h_c = H\,\Delta\rho/\rho_a, \tag{5}$$

where $\Delta\rho$ is the difference between the density of the asthenosphere and the crust, ρ_a and ρ_c, respectively.

It has long been known that to a first approximation, P wave speed is linearly related to density for most crustal rocks (Birch's law [*Birch*, 1961]). Based on a larger set of measurements, this rule has been updated as the Nafe-Drake relationship [*Ludwig et al.*, 1970; *Brocher*, 2005]. This relationship reduces the uncertainty in estimating h_c, even if there are trade-offs between H and V_P (as is the case in, for instance, reflection seismology), because two effects partially offset each other in the product $H\,\Delta\rho$ (equation (5)). For instance, an overestimate of crustal V_P obviously underestimates $\Delta\rho$ but overestimates H (e.g., equation (1)).

In particular, errors in h_c are reduced significantly when the relationship between H and V_P are constrained by VDSS (equation (1); Figure 5). Using the Nafe-Drake relationship of *Brocher* [2005], for a nominal model of crust where H and V_P are 40 km and 6.3 km/s, respectively, a deviation of 0.1 km/s in V_P will lead to an error of ~300 m in h_c, if H and V_P are unrelated. In contrast, the error in h_c is reduced by almost an order of magnitude—to a negligible value of only ~40 m—when these two quantities are interdependent via equation (1).

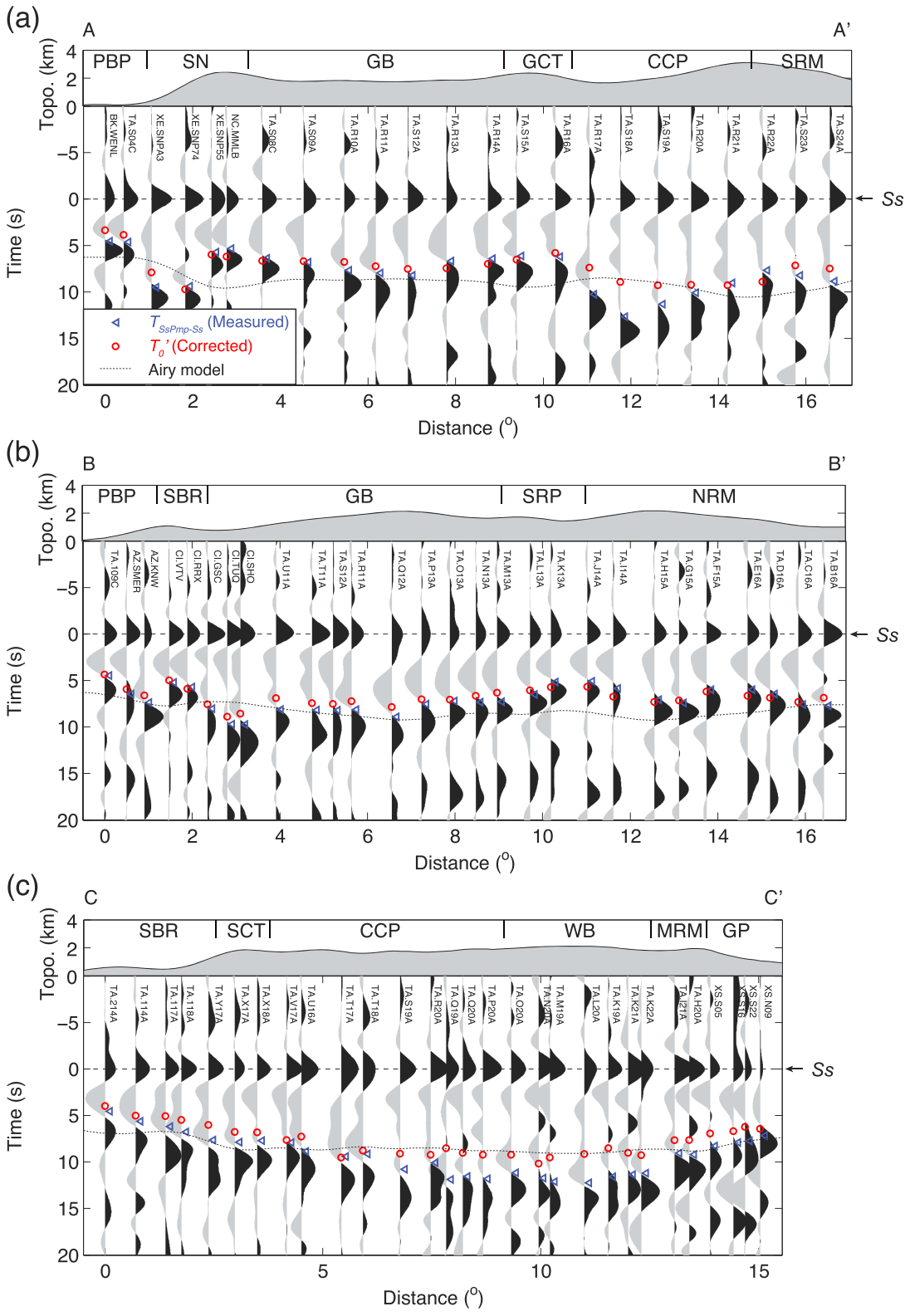

Figure 4. Three VDSS profiles across various physiographic provinces using the vertical component of *S* wave trains. (a)-(c) are along profiles AA', BB' and CC' in Figure 3, respectively. Seismograms, each labeled by its station code, are aligned along the peaks of the *Ss* phase. Left-pointing triangles mark the arrivals of the *SsPmp* phase as determined by correlation with synthetic seismograms. Red circles mark the arrival of the *SsPmp* phase, after corrections for traveltime residuals of the *Ss* phase and normalizations to a common *S* wave ray parameter (0.1316 s/km). Dotted curves mark crustal thickness predicted by Airy isostasy using the reference model described in Table S1 [*Molnar et al.*, 1993]. The seismograms are processed in the same manner as those shown in Figure 2c. See Figure 1 for abbreviations of physiographic provinces.

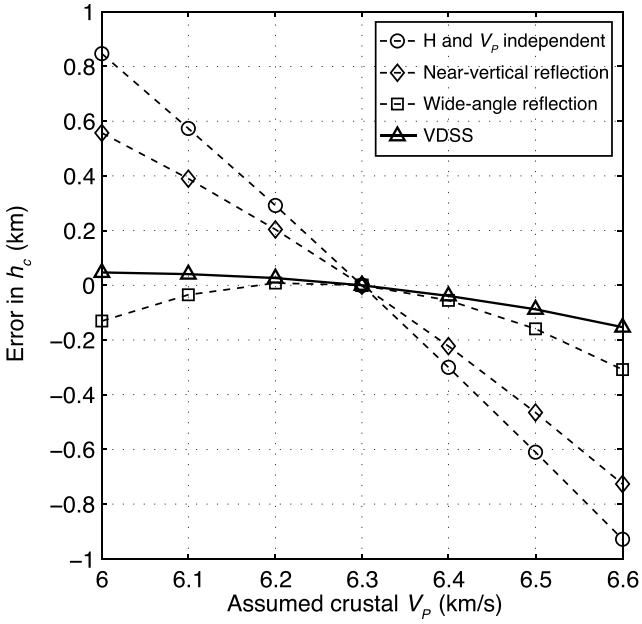

Figure 5. Estimated errors in crustal support of surface topography (h_c) caused by variations in crustal V_P. The empirical Nafe-Drake relationship is used to relate V_P to density [*Brocher*, 2005]. True values of crustal thickness (H) and V_P are 40 km and 6.3 km/s, respectively.

The only other method that gives a comparable result is conventional wide-angle reflection or deep seismic sounding (DSS). This is hardly surprising since VDSS is akin to DSS, except for the use of virtual seismic sources from natural earthquakes instead of active sources. The slight difference seen in Figure 5 between the two approaches stems from equation (1), which takes into account the fact that in VDSS the *S*-leg of the *Ss* phase travels a slightly longer path in the uppermost mantle that that of the *SsPmp*. Notice that near-vertical seismic reflection contributes only slightly to the reduction of error in h_c, because in this case the traveltime is simply the ratio between H and V_P (Figure 5).

4.2. Residual Topography

Residual topography can be defined as the difference between observed elevation and that expected from crustal buoyancy alone (equation (5)). Since estimating h_c from results of VDSS is relatively insensitive to the actual value of crustal V_P, we use a constant crustal V_P of 6.3 km/s and the corresponding value of H for each measured value of T_0'. To compare h_c derived from VDSS with actual topography, we first apply a low-pass filter to the latter, with a cutoff wavelength of 200 km (Figure 1). This procedure largely removes the component of topography supported by plate flexure, as the effective elastic thickness of the western U.S. is generally small ($<$30 km) [*Lowry and Perez-Gussinye*, 2011].

Second, one needs to choose a value for h_0, the depth of the asthenospheric geoid, or the hypothetical free surface of the asthenosphere, below a point on land that is at sea level. The predicted elevation from crustal buoyancy is then simply $(h_c - h_0)$ [*Lachenbruch and Morgan*, 1990]. A closely related parameter is D_0, the distance to the asthesnosphere geoid beneath the hydrogeoid where seawater is directly loading the asthenosphere. *Lachenbruch and Morgan* [1990] used values of relevant parameters for the mid-ocean ridge to estimate D_0, whose value, in turn, leads to an estimate of about 2.4 km for h_0. Notice that h_0 is a constant and does not affect lateral variations in residual topography.

Following the same convention of presentation as in Figure 3, the resulting distribution of residual topography is shown in Figure 6a. For ease of visualization, we also plot an interpolated version in Figure 6b. Notice that for a reference continental lithosphere under isostatic equilibrium and at zero elevation—that is, the common reference of Airy isostasy—the value of predicted elevation from crustal buoyancy $(h_c - h_0)$ is greater than zero, because crustal buoyancy must counteract the negative buoyancy of the lithospheric mantle. Consequently, the residual topography would be negative. Using a reference crustal thickness of 35 km [*Molnar et al*., 1993], the negative buoyancy exerted by the lithospheric mantle reduces by about 2 km the expected topography from crustal buoyancy alone. Therefore, for continental lithosphere under classic Airy isostasy, one would expect a residual topography of approximately −2 km (supporting information).

The main source of uncertainty in residual topography is associated with T_0'. As mentioned earlier, the typical error for measuring $T_{SsPmp\text{-}Ss}$ is usually within ±0.4 s (one standard deviation). However, errors in the "static" correction (Δt in equation (3)) are difficult to evaluate and may also vary laterally. Assuming a combined one standard deviation of ±0.6 s in T_0', the uncertainty of residual topography is around ±450 m (at 68% confidence interval). Another source of uncertainty lies in lateral variations in crustal V_P. This effect is generally

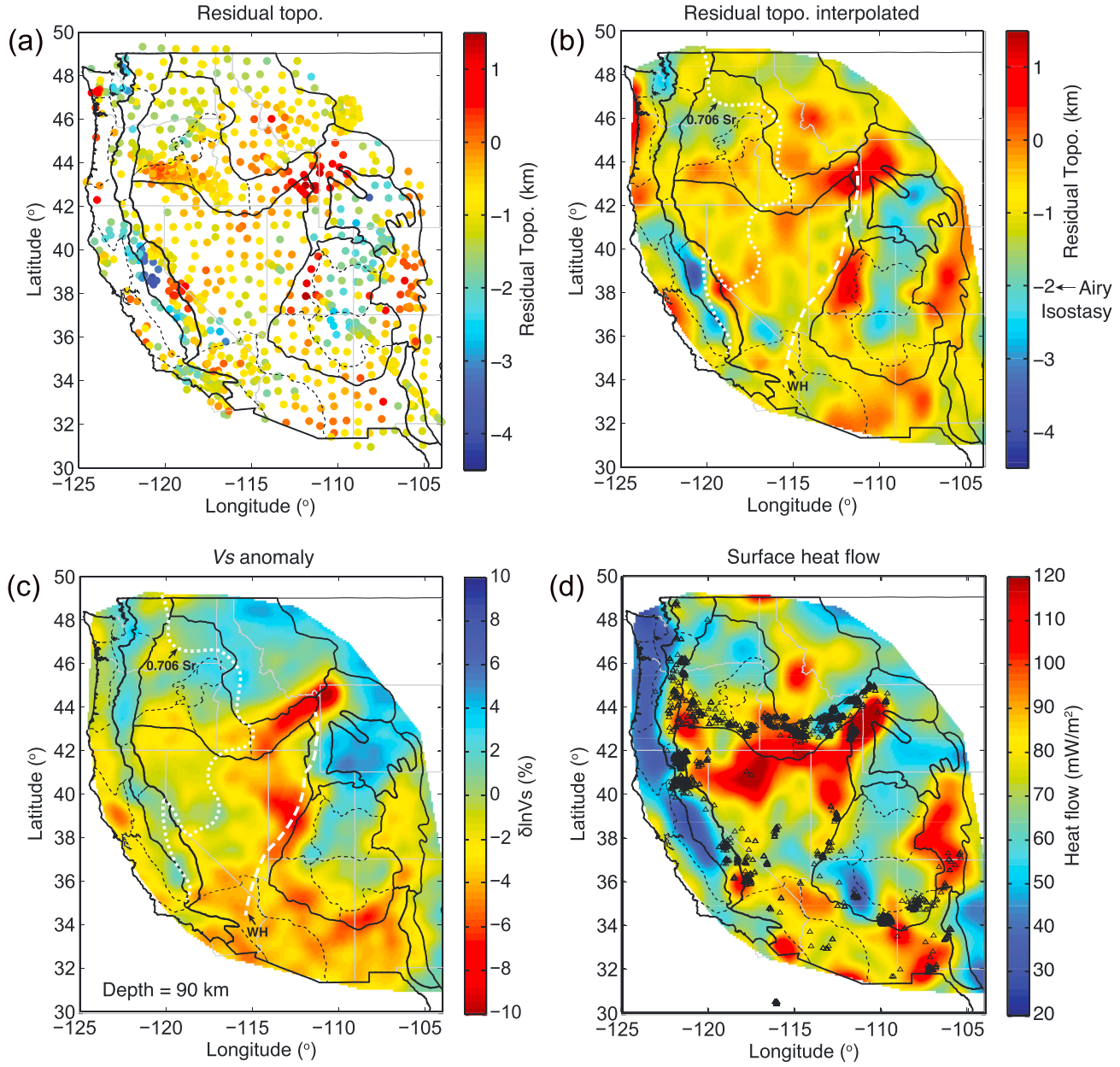

Figure 6. Maps showing (a) uninterpolated and (b) interpolated residual topography in the western United States. (c) Perturbations in *S* wave speed at a depth of 90 km from teleseismic body wave tomography [*Schmandt and Humphreys*, 2010]. In Figures 6b and 6c, we also mark the Wasatch hinge line (WH; white dashed curve), approximately the eastern limit of significant extension in the North American cratonic basement, and the eastern limit of oceanic terranes (white dotted curve), as inferred from a threshold value of 0.706 in the initial ratios of $^{87}Sr/^{86}Sr$ (modified from *DeCelles* [2004]). (d) Smoothed values of observed surface heat flows, after filtering with a cutoff wavelength of 200 km (based on the compilation of *Blackwell and Richards* [2004]). Open triangles mark locations of recent basaltic volcanism (<5 Myr; data from North American Volcanic and Intrusive Rock Database, http://www.navdat.org/).

small (Figure 5): even with a difference of ±0.2 km/s in V_P, the uncertainty in residual topography is only about ±100 m. A final source of uncertainty lies in the scaling between crustal V_P and density. We estimate that the resulting uncertainty in residual topography is about ±300 m (supporting information). Notice that this uncertainty is unlikely to affect significantly our results on relative residual topography, unless there are strong lateral variations in crustal lithology.

Lateral variations in residual topography are significant in many parts of the western U.S., such as the contrast between the interiors and the margins of the Colorado Plateau and the Wyoming Basin (Figures 6a and 6b).

On average, in the central Colorado Plateau and the Wyoming Basin, residual topography is about −2 km, indicating that these regions are close to Airy isostasy (Figures 4a and 4c). However, along margins of the Colorado Plateau (except for its northern margin) and in the Yellowstone region, residual topography fluctuates between −0.5 and 0.5 km (Figures 6a and 6b), indicating a substantial amount of additional mantle support of topography.

Farther to the west, residual topography of the Great Basin mostly ranges from −1.0 to 0.5 km. Here the lateral variations correlate with surface topography (cf. Figures 1 and 6b), as values of T_0' are fairly uniform (Figure 3). Higher values of residual topography (0 ~ 0.5 km) tend to concentrate in the surroundings of the Great Basin, such as the Eastern Snake River Plain, the High Lava Plains, and the eastern flank of the Sierra Nevada.

4.3. Comparison With Other Geophysical Measurements

Through the Nafe-Drake relationship the effect of crustal buoyancy is fully included in our estimates of residual topography. Lateral variations in residual topography thus point to heterogeneities in the mantle, and it is natural to compare our results with independently identified mantle heterogeneity. Figure 6c shows the lateral variation of *S* wave speed (ΔV_S) at a depth of 90 km inferred from teleseismic body wave tomography [*Schmandt and Humphreys*, 2010]. Since the pattern of ΔV_S varies only slightly between depths of 60 km and 120 km, we assume that the distribution shown in Figure 6c is representative of the averaged ΔV_S for the upper mantle (although we realize that some of this similarity may result from vertical smearing in the tomography results).

East of 114°W, the overall patterns of residual topography are correlated with ΔV_S. Both quantities show distinct margins surrounding the central Colorado Plateau and the Wyoming Basin. The two most prominent regions of high residual topography, the Yellowstone-Eastern Snake River Plain system and the Great Basin-Colorado Plateau transition, correlate with areas where ΔV_S is the lowest, albeit with an apparent geographic shift in the overall patterns (cf. Figures 6b and 6c). In the southern Rocky Mountains, high residual topography is also evident, but the amplitude of negative ΔV_S is moderate.

West of 114°W the situation is different. Here fluctuations in residual topography have a characteristic length of about 200 km. We note that this feature is not an artifact of filtering, and changing to lower cutoff wavelengths of 50 km or 100 km does not affect the outcome. Overall, large amplitudes of residual topography are isolated, such as near the Idaho batholith, in the Death Valley, and near the northern central Sierra Nevada (Figures 6a and 6b). Intriguingly, except at the northern margin of the Great Basin, there are no corresponding anomalies of ΔV_S in these regions. Between latitudes of 37°N and 47°N, a sequence of five relative highs roughly follow the eastern limit of oceanic terranes as inferred from a threshold value of 0.706 in the initial ratios of $^{87}Sr/^{86}Sr$ (marked as 0.706 Sr_i in Figure 6b; [*DeCelles*, 2004]). However, this relationship does not hold beyond this corridor of latitudes.

We note that the lateral transition between these two regimes—from large-scale, correlated variations in residual topography and ΔV_S in the east to smaller-scale variations in residual topography without corresponding changes in ΔV_S in the west—roughly coincides with the Wasatch hinge line, or the eastern limit of Cenozoic extension in the Precambrian crystalline basement (Figure 6b) [*DeCelles*, 2004].

Other quantities to be compared with residual topography are measurements of surface heat flows [*Blackwell and Richards*, 2004] and the distribution of recent basaltic eruptions (<5 Myr; Figure 6d; data from http://www.navdat.org/). In places, particularly east of 114°W, high heat flow and abundant basaltic eruptions often accompany significant residual topography (e.g., in the Yellowstone region). This relationship is tenuous, however, and since heat flow is not easy to interpret, we did not pursue this comparison further.

Since it is generally accepted that the upper mantle beneath the western U.S. is warm [*Thompson and Burke*, 1974], thermal anomalies seem the most likely source of static or dynamic buoyancy in the mantle. The low spatial correlation between residual topography and ΔV_S in the upper mantle suggests, however, that petrological heterogeneities also play an important role, especially west of the Wasatch hinge line.

5. Further Constraints on Crustal Properties

In addition to constraining crustal buoyancy, VDSS can provide information on V_P (equation (1)), which is an important proxy for bulk crustal properties. As is the case for all seismic reflection methods, determination of crustal thickness relies on estimates of average crustal V_P (and vice versa). One way of resolving this trade-off

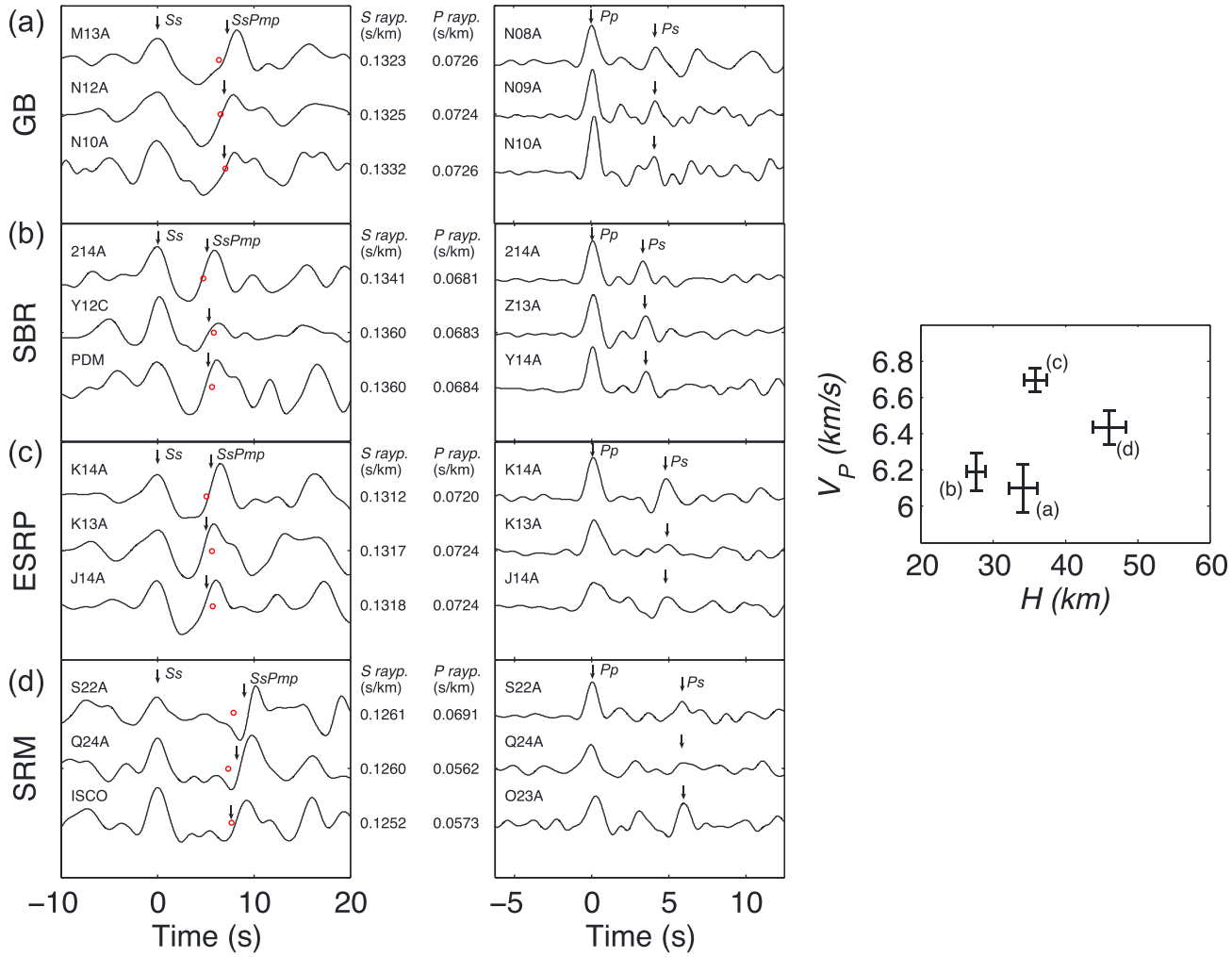

Figure 7. Examples of waveforms used in the joint analyses of VDSS (left column) and CRFs (middle column) in four physiographic provinces: (a) Great Basin (GB), (b) Southern Basin and Range (SBR), (c) Eastern Snake River Plain (ESRP), and (d) Southern Rocky Mountains (SRM). Arrows mark arrival times of key seismic phases. Circles in the left column mark the arrivals of the *SsPmp* phase after corrections as done in Figure 4. For VDSS, the seismograms are processed in the same manner as those shown in Figure 2c. Details of data processing for CRFs can be found in the supporting information. The right column shows the average crustal thickness and V_P for selected stations in each subprovince. Bars represent one standard deviation of error resulting from uncertainties in V_P/V_S according to an updated report of *Lowry and Perez-Gussinye* [2011].

is through a joint analysis of VDSS and CRFs. However, a comprehensive scan of CRFs (see supporting information) [*Crotwell and Owens*, 2005] shows that for many stations in the western U.S., *P*-to-*S* conversions across the Moho (phase *Ps*) are either very weak or heavily contaminated by reverberations from shallow structures (e.g., Figure S2). Thus, we limit such joint analyses to high-quality CRFs only.

In each (sub)physiographic province we select three nearby stations at which the primary *Ps* phase of CRF is readily identified. We then measure the time difference between phases *Ps* and *Pp* ($T_{Ps\text{-}Pp}$) and combine these data with the nearest measurements of T_0' to estimate both crustal thickness and crustal V_P (see supporting information for details). Figure 7 shows corresponding waveforms of reliable VDSS and CRFs in selected locations from four different subprovinces (see Figure 3 for exact locations). Values of crustal thickness and V_P estimated from VDSS and CRF are then averaged among each group of three stations (Figures 7 and S3; with error bars representing one standard deviation due to uncertainties in V_P/V_S ratios from an updated result of *Lowry and Perez-Gussinye* [2011]).

5.1. Basin and Range Province

In the northern part of the Great Basin (GB) and in the central part of the southern Basin and Range province (SBR), the phase *Ps* analyzed has high signal-to-noise ratios (Figure 7) and the joint analysis of VDSS and CRFs

resulted in V_P of 6.10 ± 0.14 km/s and 6.19 ± 0.11 km/s, respectively (see Figure 3 for locations). Such values are lower than the global average of 6.45 ± 0.23 km/s [*Christensen and Mooney*, 1995] but are roughly consistent with compilations in the Basin and Range province as a whole, where a number of seismic refraction profiles have been carried out [*Chulick and Mooney*, 2002]. Near-surface sediments and volcaniclastic deposits are likely causes of the low values of overall V_P here. For example, *Lerch et al.* [2007] reported thick layers of such materials (~2 km), characterized by particularly low V_P (<3 km/s) and low density (<2300 kg/m^3), in the northwestern Great Basin, close to our study region in the northern part of this basin.

The mean crustal thickness inferred here is roughly consistent with that estimated from joint inversion of CRFs and surface waves in the same regions [*Shen et al.*, 2013]. In the northern Great Basin, however, most previous studies focusing on CRFs suggest a thinner crust (25 ~ 30 km) both to the east southeast and the west southwest of our samples (~34 km) [*Lowry and Perez-Gussinye*, 2011; *Gilbert*, 2012; *Levander and Miller*, 2012; *Shen et al.*, 2013], even though our T_0' measurements are quite uniform throughout the Great Basin (Figure 3). We note that such differences mainly occur at places where the *Ps* phase is weak [*Shen et al.*, 2013, Figure 10b]. In other words, the impedance contrast across the Moho is low in these locations, suggesting a gradual crust-mantle transition. Indeed, seismic refraction profiles in the western Basin and Range province (from about 119°W to 116°W along the 39.5°N parallel) reveal a lens of transitional materials between typical crustal rocks and the mantle [*Thompson et al.*, 1989]. The base of this lens is at a depth of about 34.5 km, consistent with our sampled values of the overall crustal thickness. Indeed, a long reflection transect along the 40°N parallel during the COCORP (the COnsortium for COntinental Reflection Profiling) Project (shaded box in Figure 3 [*Klemperer et al.*, 1986]) found no obvious fluctuations in crustal thickness across the Great Basin.

5.2. Regions Surrounding the Great Basin

The mean crustal thicknesses inferred here are 36 km, 33 km, and 32 km in the Eastern Snake River Plain, the High Lava Plains, and the Great Basin-Colorado Plateau transition, respectively. Our results suggest that there are no significant differences in crustal thickness between the margins and the interior of the Great Basin. However, values of V_P in the surrounding regions are generally greater than that in the Basin and Range province. An extreme case occurs in the Eastern Snake River Plain, where the average crustal V_P reaches ~6.70 ± 0.07 km/s (Figure 7b). Somewhat lower values of ~6.37 ± 0.10 km/s are found both in the High Lava Plains and the Great Basin-Colorado Plateau transition (Figure S3).

These observations cannot be explained simply by a lack of low-velocity sediments or drastic reductions in crustal temperature. In fact, surface heat flow is generally high in these areas (Figure 6d) [*Blackwell and Richards*, 2004]. Likewise, the sedimentary covers above the Eastern Snake River Plain and the High Lava Plains are thick, a result of repeated eruptions of bimodal volcanism since the Miocene [*Sparlin et al.*, 1982; *Jordan et al.*, 2004]. Previously, a high-velocity middle crustal layer was detected by seismic refraction surveys and interpreted as a pervasive intrusion of mafic material into the crust beneath the Eastern Snake River Plain [*Sparlin et al.*, 1982]. As such, a plausible cause for elevated V_P is magmatic modification and densification of the crust by materials derived from the upper mantle.

5.3. Southern Rocky Mountains and the Colorado Plateau

Our estimate of crustal thickness under the Southern Rocky Mountains (~46 km; Figures 1 and 7d) is smaller than expected from an average elevation of about 3 km but consistent with that of other studies [*Hansen et al.*, 2013]. In view of the high surface heat flow (Figure 6d) [*Blackwell and Richards*, 2004], magmatic modification of the crust seems a reasonable explanation for the elevated values of V_P (6.44 ± 0.10 km/s).

The mean crustal thickness of the central Colorado Plateau is probably slightly larger than that of the Southern Rockies. Because of weak *P*-to-*S* conversions [*Bashir et al.*, 2011; *Shen et al.*, 2013], there are no reliable CRFs to constrain V_P in this region (Figure S3), but a value of 6.3 km/s inferred (for the entire plateau) from the compilation of *Chulick and Mooney* [2002] yields a crustal thickness of ~50 km. Under the same assumption, crustal thickness of the Wyoming Basin is estimated at ~52 km.

6. Conclusions

Application of virtual deep seismic sounding to data from about 1000 broadband seismic stations reveals significant (lateral) variations in residual topography and, by implication, mantle support of topography in

the western U.S. Cordillera. For instance, mantle support is required to explain the topography along the periphery of the Colorado Plateau and around the Wyoming craton, whereas crustal buoyancy (that is, traditional isostasy) is sufficient to maintain observed elevations in the interior of these stable geological units.

East of the Wasatch hinge line (roughly along the 114°W meridian), high residual topography correlates with low seismic wavespeed in the upper mantle. This correlation (and high surface heat flow) is consistent with anomalously high mantle temperatures. Such a correlation does not exist west of the Wasatch line, suggesting that residual topography here cannot be explained by thermal anomalies alone and that variations in petrology or composition or dynamic forces must also play a role.

Joint analyses of virtual deep seismic sounding and conventional receiver functions are useful in resolving the trade-off between crustal thickness and the overall speed of *P* wave in the crust. For the latter, values as low as 6.1 km/s and as high as 6.7 km/s are found at selected locations where conventional receiver functions are reliable. Such high values suggest modification of the crust by magmatic materials derived from the mantle.

Acknowledgments
All broadband seismic waveforms are from the IRIS Data Services. Constructive reviews by K. Liu, an anonymous reviewer, and Editor P. Tregoning helped improve the manuscript. Data used in this study are available from the authors upon request (yucq@mit.edu). This study is supported by grant DE-NA0001523 from the U.S. Department of Energy (van der Hilst) and "985" funds through the Chinese Ministry of Education (Chen).

References

Ammon, C. J. (1991), The isolation of receiver effects from teleseismic *P* waveforms, *Bull. Seismol. Soc. Am.*, *81*(6), 2504.
Bashir, L., S. S. Gao, K. H. Liu, and K. Mickus (2011), Crustal structure and evolution beneath the Colorado Plateau and the southern Basin and Range Province: Results from receiver function and gravity studies, *Geochem. Geophys. Geosyst.*, *12*, Q06008, doi:10.1029/2011GC003563.
Becker, T. W., C. Faccenna, E. D. Humphreys, A. R. Lowry, and M. S. Miller (2013), Static and dynamic support of western United States topography, *Earth Planet. Sci. Lett.*, *402*, 234–246.
Birch, F. (1961), The velocity of compressional waves in rocks to 10 kilobars, part 2, *J. Geophys. Res.*, *66*(7), 2199–2224, doi:10.1029/JZ066i007p02199.
Blackwell, D., and M. Richards (2004), Geothermal map of North America, Am. Assoc. of Petrol. Geol., Tulsa, Okla., scale: 1:6,500,000.
Brocher, T. M. (2005), Empirical relations between elastic wavespeeds and density in the Earth's crust, *Bull. Seismol. Soc. Am.*, *95*(6), 2081–2092.
Buehler, J. S., and P. M. Shearer (2010), *Pn* tomography of the western United States using USArray, *J. Geophys. Res.*, *115*, B09315, doi:10.1029/2009JB006874.
Burchfiel, B., D. Cowan, and G. Davis (1992), Tectonic overview of the Cordilleran orogen in the western United States, in *Cordilleran Orogen: Conterminous US*, vol. 3, pp. 407–479, Geol. Soc. of Am., Geology of North America, Boulder, Colo.
Burdick, S., R. D. van der Hilst, F. L. Vernon, V. Martynov, T. Cox, J. Eakins, G. H. Karasu, J. Tylell, L. Astiz, and G. L. Pavlis (2010), Model update January 2010: Upper mantle heterogeneity beneath North America from traveltime tomography with global and USArray transportable array data, *Seismol. Res. Lett.*, *81*(5), 689–693.
Christensen, N., and W. Mooney (1995), Seismic velocity structure and composition of the continental crust: A global view, *J. Geophys. Res.*, *100*(B6), 9761–9788, doi:10.1029/95JB00259.
Chulick, G. S., and W. D. Mooney (2002), Seismic structure of the crust and uppermost mantle of North America and adjacent oceanic basins: A synthesis, *Bull. Seismol. Soc. Am.*, *92*(6), 2478–2492.
Crotwell, H. P., and T. J. Owens (2005), Automated receiver function processing, *Seismol. Res. Lett.*, *76*(6), 702–709.
DeCelles, P. G. (2004), Late Jurassic to Eocene evolution of the Cordilleran thrust belt and foreland basin system, western USA, *Am. J. Sci.*, *304*(2), 105–168.
Feneman, N. (1931), *Physiography of the Western United States*, 1st ed., McGraw-Hill Book Co., New York.
Gilbert, H. (2012), Crustal structure and signatures of recent tectonism as influenced by ancient terranes in the western United States, *Geosphere*, *8*(1), 141–157.
Hansen, S. M., K. G. Dueker, J. C. Stachnik, R. C. Aster, and K. E. Karlstrom (2013), A rootless rockies—Support and lithospheric structure of the Colorado Rocky Mountains inferred from CREST and TA seismic data, *Geochem. Geophys. Geosyst.*, *14*, 2670–2695, doi:10.1002/ggge.20143.
Hyndman, R., and C. Currie (2011), Why is the North America Cordillera high? Hot backarcs, thermal isostasy, and mountain belts, *Geology*, *39*(8), 783–786.
Jordan, B. T., A. L. Grunder, R. A. Duncan, and A. L. Deino (2004), Geochronology of age-progressive volcanism of the Oregon High Lava Plains: Implications for the plume interpretation of Yellowstone, *J. Geophys. Res.*, *109*, B10202, doi:10.1029/2003JB002776.
Klemperer, S. L., T. Hauge, E. Hauser, J. Oliver, and C. Potter (1986), The Moho in the northern Basin and Range province, Nevada, along the COCORP 40 N seismic-reflection transect, *Geol. Soc. Am. Bull.*, *97*(5), 603–618.
Lachenbruch, A. H., and P. Morgan (1990), Continental extension, magmatism and elevation; formal relations and rules of thumb, *Tectonophysics*, *174*(1), 39–62.
Lerch, D., S. Klemperer, J. Glen, D. Ponce, E. Miller, and J. Colgan (2007), Crustal structure of the northwestern Basin and Range Province and its transition to unextended volcanic plateaus, *Geochem. Geophys. Geosyst.*, *8*, Q02011, doi:10.1029/2006GC001429.
Levander, A., and M. S. Miller (2012), Evolutionary aspects of lithosphere discontinuity structure in the western US, *Geochem. Geophys. Geosyst.*, *13*, Q0AK07, doi:10.1029/2012GC004056.
Levandowski, W., C. H. Jones, W. Shen, M. H. Ritzwoller, and V. Schulte-Pelkum (2014), Origins of topography in the western US: Mapping crustal and upper mantle density variations using a uniform seismic velocity model, *J. Geophys. Res. Solid Earth*, *119*, 2375–2396, doi:10.1002/2013JB010607.
Lin, F.-C., B. Schmandt, and V. C. Tsai (2012), Joint inversion of Rayleigh wave phase velocity and ellipticity using USArray: Constraining velocity and density structure in the upper crust, *Geophys. Res. Lett.*, *39*, L12303, doi:10.1029/2012GL052196.
Lowry, A. R., and M. Perez-Gussinye (2011), The role of crustal quartz in controlling Cordilleran deformation, *Nature*, *471*(7338), 353–357.
Lowry, A. R., N. M. Ribe, and R. B. Smith (2000), Dynamic elevation of the Cordillera, western United States, *J. Geophys. Res.*, *105*(B10), 23,371–23,390, doi:10.1029/2000JB900182.
Ludwig, W. J., J. E. Nafe, and C. L. Drake (1970), Seismic refraction, *The Sea*, *4*(Part 1), 53–84.

Molnar, P., P. England, and J. Martinod (1993), Mantle dynamics, uplift of the Tibetan Plateau, and the Indian monsoon, *Rev. Geophys.*, *31*(4), 357–396, doi:10.1029/93RG02030.

Randall, G. (1989), Efficient calculation of differential seismograms for lithospheric receiver functions, *Geophys. J. Int.*, *99*(3), 469–481.

Schmandt, B., and E. Humphreys (2010), Complex subduction and small-scale convection revealed by body-wave tomography of the western United States upper mantle, *Earth Planet. Sci. Lett.*, *297*(3-4), 435–445, doi:10.1016/j.epsl.2010.06.047.

Schulte-Pelkum, V., G. Biasi, A. Sheehan, and C. Jones (2011), Differential motion between upper crust and lithospheric mantle in the central Basin and Range, *Nat. Geosci.*, *4*(9), 619–623.

Shen, W., M. H. Ritzwoller, and V. Schulte-Pelkum (2013), A 3-D model of the crust and uppermost mantle beneath the central and western US by joint inversion of receiver functions and surface wave dispersion, *J. Geophys. Res. Solid Earth*, *118*, 262–276, doi:10.1029/2012JB009602.

Sheriff, R. E., and L. P. Geldart (1995), *Exploration Seismology*, Cambridge Univ. Press, Cambridge.

Sparlin, M. A., L. Braile, and R. Smith (1982), Crustal structure of the eastern Snake River Plain determined from ray trace modeling of seismic refraction data, *J. Geophys. Res.*, *87*(B4), 2619–2633, doi:10.1029/JB087iB04p02619.

Thompson, G. A., and D. B. Burke (1974), Regional geophysics of the Basin and Range province, *Annu. Rev. Earth Planet. Sci.*, *2*, 213–238.

Thompson, G. A., R. Catchings, E. Goodwin, S. Holbrook, C. Jarchow, C. Mann, J. McCarthy, and D. Okaya (1989), Geophysics of the western Basin and Range province, *Geol. Soc. Am. Mem.*, *172*, 177–204.

Tseng, T.-L., W.-P. Chen, and R. L. Nowack (2009), Northward thinning of Tibetan crust revealed by virtual seismic profiles, *Geophys. Res. Lett.*, *36*, L24304, doi:10.1029/2009gl040457.

USGS (1993), *Digital Elevation Models: Data Users Guide 5*, U.S. Gov't Print. Off., Washington, D. C.

Wernicke, B. P., P. C. England, L. J. Sonder, and R. L. Christiansen (1987), Tectonomagmatic evolution of Cenozoic extension in the North American Cordillera, *Geol. Soc. London Spec. Publ.*, *28*(1), 203–221.

Yang, Y., M. H. Ritzwoller, F.-C. Lin, M. Moschetti, and N. M. Shapiro (2008), Structure of the crust and uppermost mantle beneath the western United States revealed by ambient noise and earthquake tomography, *J. Geophys. Res.*, *113*, B12310, doi:10.1029/2008JB005833.

Yu, C.-Q., W.-P. Chen, J.-Y. Ning, K. Tao, T.-L. Tseng, X.-D. Fang, Y. John Chen, and R. D. van der Hilst (2012), Thick crust beneath the Ordos plateau: Implications for instability of the North China craton, *Earth Planet. Sci. Lett.*, *357*, 366–375, doi:10.1016/j.epsl.2012.09.027.

Yu, C.-Q., W.-P. Chen, and R. D. van der Hilst (2013), Removing source-side scattering for virtual deep seismic sounding (VDSS), *Geophys. J. Int.*, *195*(3), 1932–1941, doi:10.1093/gji/ggt359.